Appendix A

Sequential Buckle Characteristics and Mechanical Response of VACNT Foams Synthesized Using Fixed-catalyst CVD Process[7]

In this chapter, we present the mechanical response and a unique buckling characteristic observed in vertically aligned carbon nanotube (VACNT) foams synthesized using fixed-catalyst thermal chemical vapor deposition (tCVD) process. These VACNT samples are composed of multi-walled CNTs (MWCNTs) with fewer walls and as a result have an order-of-magnitude-lower density compared to the VACNT foams synthesized using the floating-catalyst tCVD process. They present an intrinsic mass density gradient along the height that we measured using synchrotron x-ray scattering and mass attenuation. We correlate their mechanical response and their fundamental deformation mechanisms to the intrinsic density gradient and the foam morphology. We observe that the buckles formed at the external edges of the samples are much fewer and have significantly large wavelengths compared to the buckles formed inside the samples. We performed simplified Euler buckling calculations and found that the buckling modes found inside the sample are the dominant deformation mechanism that governs the measured bulk mechanical response.

A.1   Synthesis and morphological characteristics of the VACNT foams

We used a thermal chemical vapor deposition process (tCVD) to synthesize the VACNT foams on substrates with fixed-catalyst as described in Section 2.1.2. The synthesized samples had an average height of 1.02±0.076 mm and an average bulk density of 0.011±0.0031 g cm^{-3}.

We used scanning electron microscopy (SEM) and transmission electron microscopy (TEM) to characterize the morphology of the sample. The samples showed a hierarchical structure (Figure A.1) in which the macroscale VACNT foams constitute vertically aligned bundles of CNTs in the mesoscale, entangled CNTs form a forest-like system in the microscale and the individual CNTs have a multiwalled structure with number of walls varying between three and seven. The MWCNTs in the forest have average outer diameter of 8.6±1.8 nm.
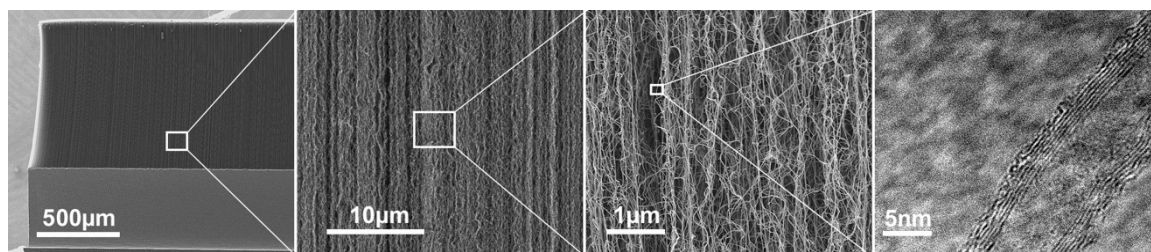

Figure A.1. The hierarchical structure of VACNT foams in which the macroscale VACNT foam constitutes vertically aligned bundles of CNTs in the mesoscale, entangled CNTs form a forest like system in the microscale and the individual CNTs have a multiwalled structure.

We performed synchrotron X-ray scattering and mass attenuation measurements to nondestructively quantify the density and alignment within VACNT foams (see section 2.2 for detailed methods). The results revealed the presence of an intrinsic mass density gradient along the height of the sample (Figure A.2 (a)). A representative sample showed a 40% density gradient with mass density varying from 0.009 to 0.015 g cm^{-3} from bottom to top of the sample and had an average bulk density of 0.012 g cm^{-3}. The Herman's orientation factor was found to be, on average, 0.31 and it increased towards the bottom of the sample, implying more vertical alignment at the bottom than the top (Figure A.2 (b)). However, the average alignment was significantly lower than that of the VACNT foams synthesized using the floating-catalyst CVD process. The floating-catalyst CVD exhibited an average orientation factor from 0.54-0.7 depending on the hydrogen concentration used during synthesis (higher hydrogen concentrations result in less alignment) [166].
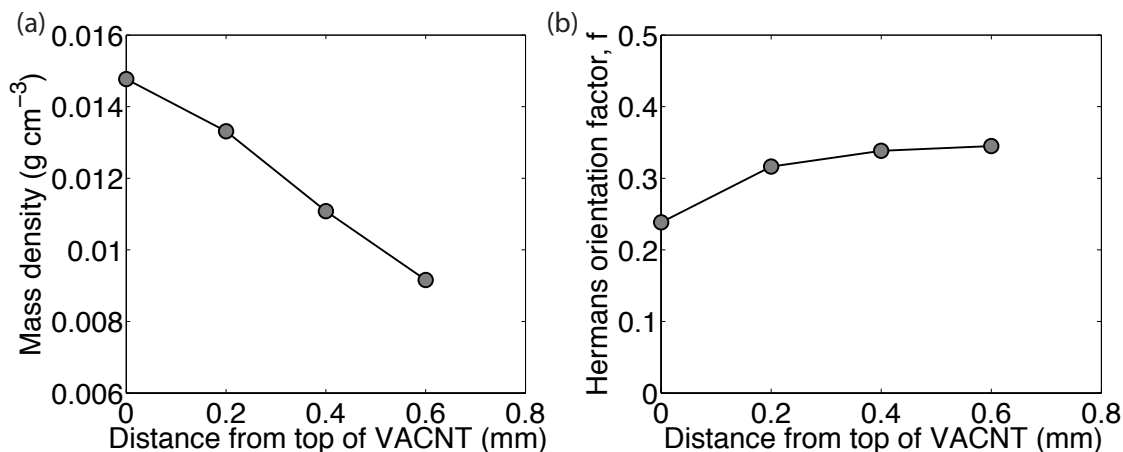
Figure A.2. Structural characteristics of the VACNT foams: **(a)** the mass density gradient along the height, from the top of the sample, **(b)** variation of the Herman's orientation factor along the height, from the top of the sample.

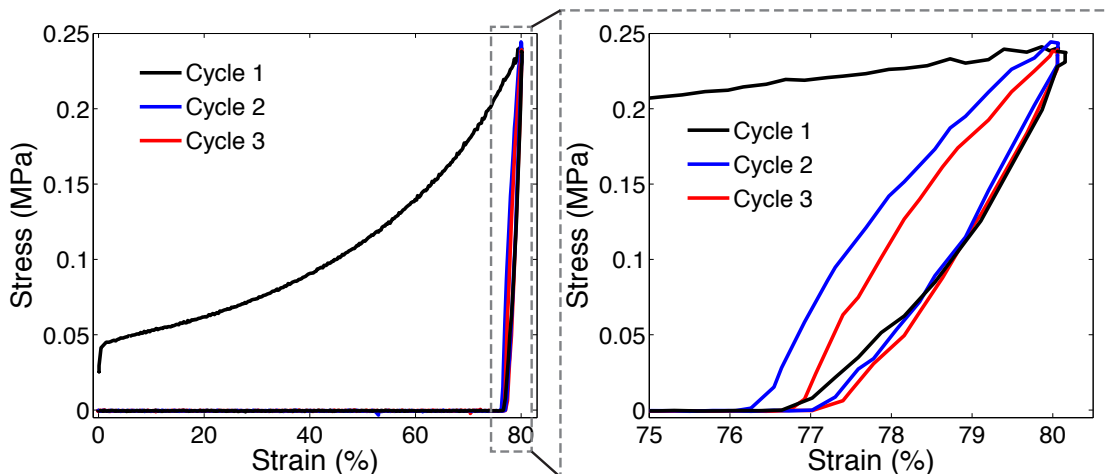## A.2 Mechanical response of the VACNT foams

Figure A.3. A characteristic stress-strain response of a VACNT foam subjected to three compressive loading-unloading cycles.

We performed quasistatic compression experiments on the VACNT foams using a commercial compression testing system (*Instron ElectroPulse E3000*) to characterize their mechanical behavior (see Section 2.3). Initially a small precompression (<0.025 MPa) was applied to ensure the whole top surface of the sample was in contact with the

loading plate. When the sample was compressed, the stress rose linearly with strain initially and then followed a nonlinear stress rise in strain as the sample was compressed to up to 80% strain (Figure A.3). Upon unloading, sample did not show any significant strain recovery (only 3.6% recovery) and remained compressed. The consecutive cycles did not show any stress rise until the loading plate came into contact with the sample and then the stress rose to the peak stress level reached at 80% strain during the first cycle. Almost all the work done during loading is dissipated by the sample and this sample dissipated 82.1 kJ m^{-3} energy in the first cycle. On average the VACNT samples dissipated 66.3±18.3 kJ m^{-3} energy in the first cycle.
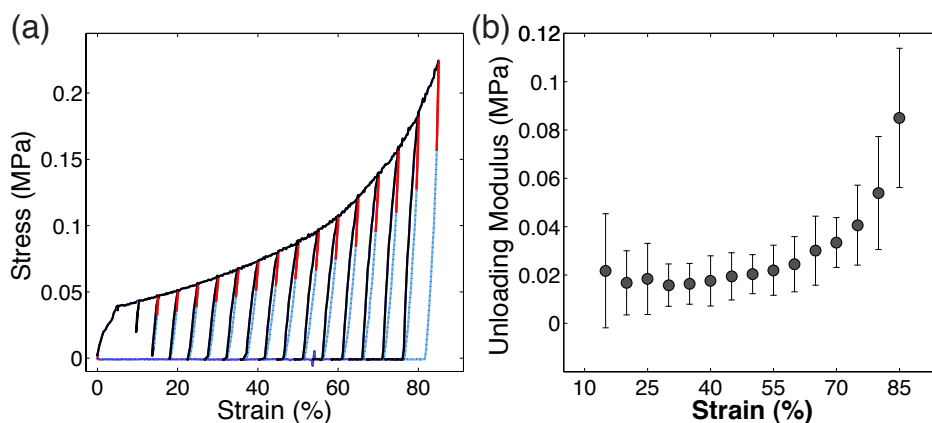
Figure A.4. (a) A characteristic stress-strain response of a VACNT sample showing the method of calculating unloading modulus. **(b)** The variation of unloading modulus of the VACNT foams with strain. Error bars represent the standard deviation of many samples tested.
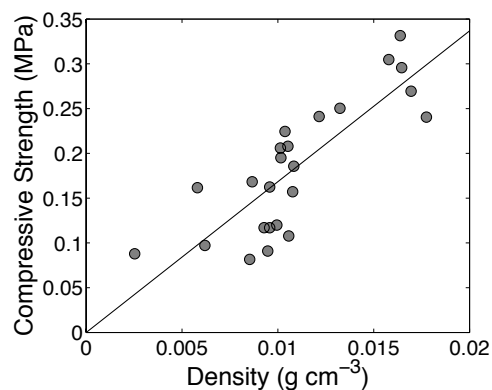
Figure A.5. The variation of the compressive strength (peak stress at 80% strain) with the bulk density of the VACNT foams.

We quantified the elastic modulus of the VACNT foam by measuring the unloading modulus at different strains as shown in the Figure A.4 (a). The unloading modulus is calculated as the slope of the initial 30% of unloading from the corresponding strain. The elastic modulus increases with the strain moderately (at ~20 kPa) up to the densification strain (~65%) and then shows a rapid increase with strain (Figure A.4 (b)). The elastic moduli is significantly affected by the variations in bulk density of the samples and the error bars in Figure A.4 (b) represent the standard deviation of several samples tested. We found that the compressive strength (peak stress at 80%) is also a function of bulk density and it showed a linear correlation with the bulk density of the samples (Figure A.5).

A.3   Characteristics of the deformations

We used high-speed microscopy for *in-situ* visualization and characterization of the deformation mechanisms during compression. When the sample is compressed, following the initial linear stress rise in strain, local buckles nucleate adjacent to the substrate and progresses laterally at first until a height segment of the sample is fully buckled and compressed. After that, the buckles progress upwards sequentially while the compressive stress rises nonlinearly. We correlate the formation of instabilities at the bottom of the sample and its progression towards the top of the sample to the intrinsic density gradient we measured using synchrotron x-ray scattering. Buckles nucleate at the bottom low-density (soft) region and progress sequentially towards the top dense region of the sample. The *in-situ* microscopy and post-compression SEM imaging revealed two interesting observations (Figure A.6): (i) the buckles always nucleate locally at several locations along the width of the sample and a particular height segment of the sample does not form a single buckle and collapse at once, (ii) the samples exhibit local buckle-induced delamination at the interface between the VACNTs and the substrate. The local variations in the morphology (density, orientation of CNTs, alignment of bundles, etc.) and non-uniformity in the height of the sample across the width may modulate the formation of the buckles locally. Further, the SEM images of onset of buckling demonstrate that

buckling in VACNT foams is a mesoscale effect coming from the collective response of the CNTs rather than a microscale effect governed by the strength of individual CNTs. The local delamination of VACNTs from the substrate under macro-compression of VACNT arrays has been observed previously and it was attributed to local stress concentrations that can impose local tensile stresses to overcome the adhesion between the VACNTs and the substrate [207].
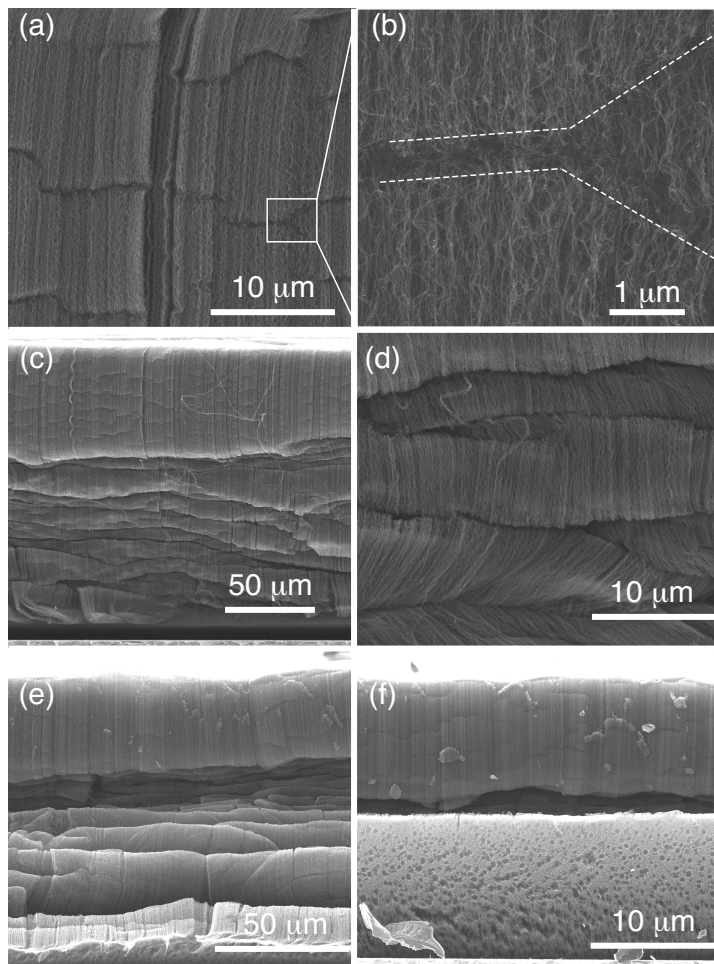

Figure A.6. (a-d) Local non-uniform buckle formation: **(a)** onset of buckling at different locations, **(b)** closer view of onset of buckling, **(c)** after several buckles have formed sequentially under compression, **(d)** closer view showing non-uniformity in the buckles. **(e-f)** Buckle induced delamination of the VACNTs from the substrate: **(e)** delamination at the interface of VACNTs and substrate, **(f)** closer view of the delaminated surface of the

VACNTs.

We observed another intriguing response from the SEM images performed on the compressed sample, on the external surface and the inside of the sample that was accessed by cutting the compressed external surface (Figure A.7). The inside of the samples present large number of buckles of much smaller wavelengths, compared to the outside edge. The source of such a large difference remains unclear and has to be verified through further experiments and analysis. One possible source could be variations in structural characteristics of the VACNTs between the central volume and the edges of the samples, when synthesized using a fixed-catalyst tCVD process. We plan to perform synchrotron x-ray scattering and mass attenuation measurements to characterize the VACNT morphology along the width of the sample to verify this phenomenon.
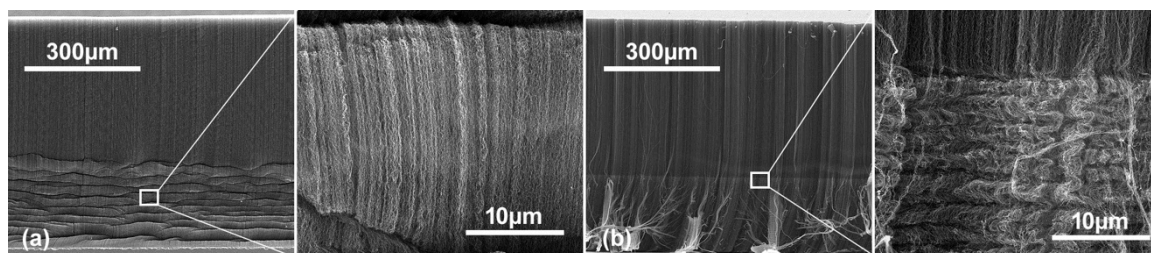

Figure A.7. Collective buckles observed **(a)** outside and **(b)** inside a VACNT foam sample. SEM images were acquired at the same scales for a side-by-side comparison.

From the *in-situ* high-speed microscope video obtained on the edge of the sample, we measured the critical onset buckling wavelengths (L_{cr}) and the buckle wavelengths after the buckle was completely formed (L_{co}), as a function of the location along the height of the sample (Figure A.8 (a)). The buckle wavelengths varied largely from sample to sample and didn't show a particular correlation with the height (Figure A.8 (b), (c)). However, we found a linear correlation between the critical onset of buckling wavelengths (L_{cr}) and the post-buckle wavelengths (L_{co}) (Figure A.8 (d)). We measured the post-compression buckle wavelength (L_{co}) inside the sample by first cutting off the edges using a razor blade and then performing SEM imaging of the internal view (Figure A.8 (e)). From Figure A.8 (f), it can be seen that the buckle wavelengths found inside the sample are much lower compared to the outside buckles. In addition, the compressed

buckle wavelengths increase with height, which could be an outcome of the increasing intrinsic density gradient along the height from the bottom of the sample.
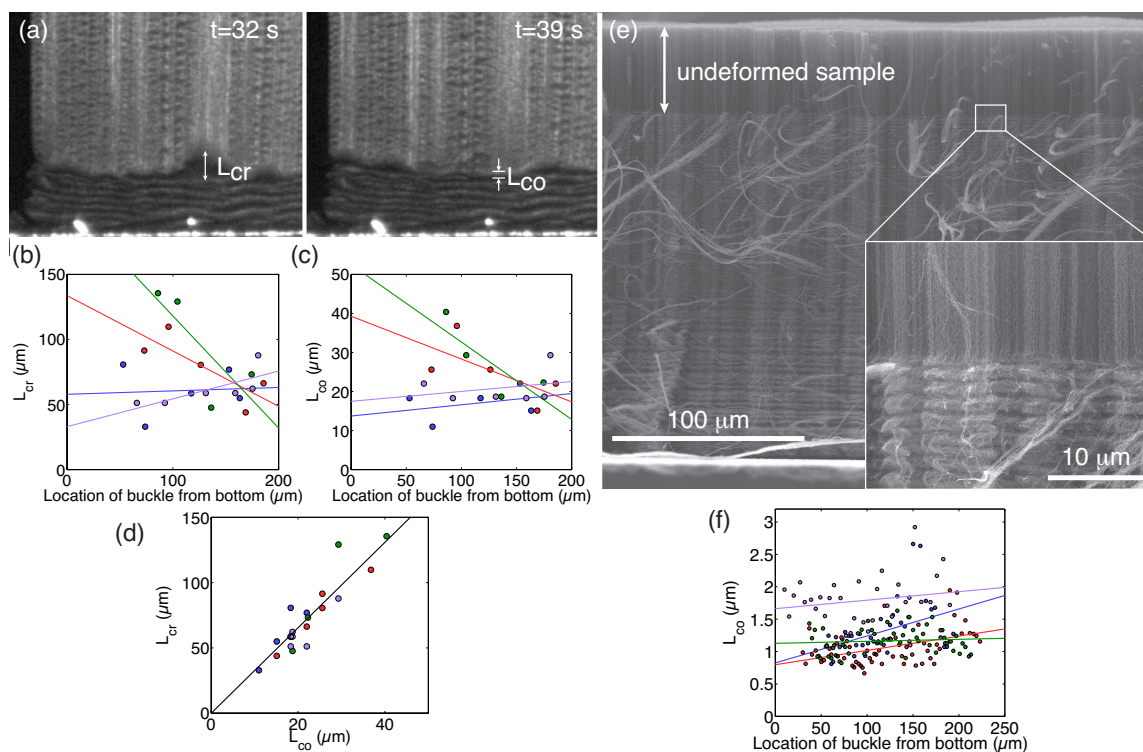

Figure A.8. (a-d) Buckle wavelengths measured outside the sample: **(a)** *in-situ* microscopy image showing the critical buckle wavelength onset of buckling (L_{cr}) and the buckle wavelength after the buckle is compressed (L_{co}), **(b)** variation of the critical buckle wavelength (L_{cr}) with location of the buckle measured from the substrate, **(c)** variation of buckle wavelength after the buckle is compressed (L_{co}) with location of the buckle measured from the substrate, and **(d)** the linear correlation between the buckle wavelength's onset of buckling and after compression. **(e-f)** Buckle wavelengths measured inside the sample: **(e)** SEM images showing large number of buckles with much lower wavelengths, and **(f)** variation of compressed buckle wavelengths (L_{co}) with location of the buckle measured from the substrate.

A.4   Simplified analysis of the buckling

We now discuss a simplified Euler buckling analysis performed to analytically find the critical buckle wavelength for an individual CNT, ignoring the entanglement and the

nearest neighbor interactions between the CNTs. Even though such an assumption is not completely justifiable, because of the entangled morphology of the VACNTs and the collective buckles observed, we found that this approximate calculation results in buckle wavelengths that closely match the internal buckle wavelengths.
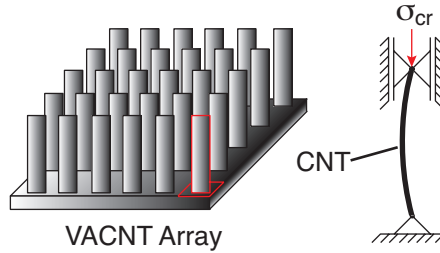

Figure A.9. A simplified Euler buckling model of the CNT in a VACNT array. A CNT is modeled as a cylindrical hollow column with pin supports in both ends.

In this simplified model, we consider a MWCNT as a hollow cylinder that is pin supported in top and bottom ends. From the TEM images of our MWCNTs, we find the average outer diameter of the CNTs (d_o) is 8.6 nm, and the inner diameter (d_i) is 5 nm. Therefore, the area moment of inertia (I) is calculated to be 237.83 nm^4 from

$$I = \pi \frac{(d_o{}^4 - d_i{}^4)}{64}. \tag{A.1}$$

The critical Euler buckling load (F_{cr}) is given by

$$F_{cr} = \frac{\pi^2 E I}{(kL)^2}, \tag{A.2}$$

where E is the elastic modulus, L is the unsupported length of the column and k is equal to 1 for a column with both ends pin supported. From the experimental measurements reported in literature for a single CNT, we find the elastic modulus to be 1 TPa [175,208]. We calculated the critical force on a single CNT from the measured critical force on the whole sample, divided by the number of CNTs in the array. We calculated the number of CNTs in the array from the measured average weight of the sample divided by the calculated average weight of a CNT. The weight of a representative individual CNT with five walls on average is calculated from the weight of the carbon atoms multiplied by the

number of carbon atoms in a CNT, assuming that the CNTs are free of any defects and have a perfect structure. This calculation showed that there are 3.38×10^9 tubes present in our sample with area (5 mm x 5 mm). Therefore the areal density of the CNTs in our VACNT sample is 1.35×10^{10} tubes cm^{-2}, which is comparable to the number density found in literature for VACNT samples synthesized with hydrogen annealed fixed-catalyst (1.84×10^{10} tubes cm^{-2} [39]).

We choose the nominal stress found at 40% strain of the sample, 0.05 MPa, as the critical stress causing bucking, since 40% strain approximately represents the section of the sample that has the value of the average bulk density along the intrinsic density gradient. Therefore, the critical force on a MWCNT is calculated as 0.37 nN, from the CNT number density and the total critical force on the sample. Therefore from Equation (A.2) the column length, L, is calculated to be 2.52 μm. Therefore the wavelength of the buckle is 5.04 μm at onset of buckling. The onset of buckling wavelength (L_{cr}) measured from the SEM images for the internal buckles, is ~8.4 μm (this L_{cr} is calculated by multiplying the compressed buckle wavelength, L_{co} by the linear correlation coefficient found between L_{co} and L_{cr} for external buckles, assuming that the correlation coefficient remains the same for inside and outside (Figure A.8 (d))). The measured onset of buckling wavelength (L_{cr}) for the externally observed buckles is ~80 μm which is nearly 16 times larger than the calculated wavelength. The close match found between the calculated and the measured internal buckle wavelengths in these approximate calculations demonstrates that the characteristic internal buckling modes found in the samples are the dominant deformation mechanisms that govern the bulk mechanical response.

A.5 Conclusions

In summary, the VACNT foams synthesized using the fixed-catalyst tCVD process have significantly low density compared to the VACNT foams synthesized using floating-catalyst samples. As a result, they present very soft mechanical responses subjected to quasistatic compression. Unlike the floating catalyst VACNT foams, these VACNT foams do not show any significant recovery upon unloading. They present progressive

sequential buckling that is governed by the intrinsic density gradient along the height. We have identified buckling with different characteristic wavelengths inside and outside the samples. The external surface of the samples presents fewer buckles with significantly larger wavelengths. From simplified Euler buckling analysis we have shown that the internal buckling modes represent the governing deformation mechanism of the bulk sample.

Appendix B

Wave Propagation in a Periodic Array of VACNT Foams Alternated with Rigid Interlayers[8]

We show a unique wave propagation characteristic in a one-dimensional periodic array of vertically aligned carbon nanotube (VACNT) foams with rigid interlayers. The effective velocity of the propagating wave in the periodic array decreases with increasing impact force. The array is excited transiently using spherical strikers launched at controlled velocities of between 1 and 8 m s^{-1}. We also show that the wave velocity is highly tunable by more than 200%, simply by applying static precompression to the system, merely between 0.28 and 2.8 MPa. We develop an analytical rate-independent hysteretic model for the VACNT foams and explain the unique wave propagation characteristics observed in the system.

B.1 Introduction.

Heterogeneous layered composites made of constituent materials with drastically different physical and mechanical properties often present intriguing physical responses. For example, forming a laminated composite using alternating hard (e.g. ceramics, metals) and soft materials (e.g. polymers) reduces the wave velocity compared to that of in the individual constituent materials [209,210]. It also takes advantage of the crack-arresting feature of the soft layer, thereby improving the penetration resistance in ballistic impacts [209]. Periodic layering of dissimilar materials also leads to interface scattering, increased shock viscosity and the formation of structured shock waves during transient excitations [210] or formation of selective frequency band gaps and wave attenuation in continuous excitations [211]. The wave characteristics in such layered media are influenced by several heterogeneity factors such as impedance mismatch between the

layers, interface density (the density of the interface area per volume), and the thickness ratio of the layers [212]. Analytical and numerical studies have proposed several ways to engineer the interlayers to enhance the wave propagation characteristics, for instance, by introducing functionally graded materials to induce time delays [213] or by introducing shape memory materials for active controlling of wave propagation [214].

Recently several periodically layered nanocomposites with superior characteristics have been fabricated for applications requiring impact and energy absorption. For example, polyurethane multiblock-segmented copolymers [215] and polystyrene-polydimethylsiloxane (PS-PDMS) diblock copolymers [113] composed of 'hard' glassy and 'soft' rubbery polymer segments have been shown to exhibit outstanding performance in high-rate compression [215] and in micro ballistic impacts [113]. Their superior performance is attributed to their nanoscale superstructures, the self-healing ability of polymers, and layer-orientation-dependent fundamental deformation mechanisms such as layer kinking, layer compression, domain fragmentation and liquid formation [113,215]. Vertically aligned carbon nanotube (VACNT) reinforced polymer sandwich composites have been shown to display high rigidity and enhanced damping in the linear dynamic regime [86]. Hybrid layered nanocomposites made by intercalating VACNTs into natural inorganic materials and tested in quasistatic compression cycles have shown compressibility up to 90% of their initial heights and ~10 times higher energy absorptions than their original constituent materials [71]. Similar multilayer arrays of VACNT foams with thin polymer (PDMS) interlayers have been shown to exhibit exceptional energy absorption in quasistatic compression cycles, ~200 times higher than those of commercial foams of similar bulk densities [72]. Introducing microstructural heterogeneities within the VACNT foams by synthesizing discrete 'soft' and 'stiff' bands has also been shown to improve the energy absorption and result in controlled deformations of the foams when impacted with a spherical striker (3.47 g) at low impact velocities (0.7-1.7 ms^{-1}) [193].

Free standing VACNT foams that have been synthesized using standard chemical vapor deposition (CVD) techniques present several unique mechanical characteristics that are desirable for protective applications and can serve as a model material for understanding

the fundamental mechanical response of fibrous hierarchical materials. When compressed, they exhibit foam-like nonlinear stress-strain responses with hysteresis loops [37]. They undergo super compressibility in quasistatic [37] and dynamic [14] compression [169] and recover most of their deformation. They dissipate energy through hysteresis [37] and survive fatigue at up to millions of compression cycles [38]. They undergo sequential collective buckling in quasistic compression [145] and exhibit shock formation when impacted at velocities higher than their critical velocity [166]. Sequential progressive buckling and the stress-strain response are highly influenced by the functionally graded properties of VACNT foams (intrinsic density and stiffness gradients) that arise from the CVD synthesis process [166,216]. It has been shown that the mechanical properties of the VACNT foams can be tailored significantly over a broad range using different synthesis techniques: for example, soft VACNT foams can be synthesized by introducing varying concentrations of hydrogen in the carrier gas [42] or very stiff VACNT foams can be synthesized through attachment of metal oxide nanoparticles to the CNTs [44].

Here, we present the experimental and numerical studies of wave propagation in a one-dimensional periodic array of VACNT foams with rigid interlayers. We demonstrate highly tunable, unique wave propagation characteristics in the multilayer array. We use a rate-independent hysteretic model to describe the VACNT response and model the unique wave propagation characteristics observed in the experiments using a chain of masses connected by the proposed VACNT model.

B.2   Experimental setup and methods

B.2.1 Synthesis of VACNT foams

We synthesized the VACNT foams using a floating catalyst thermal CVD process described in Section 2.1.1. Resultant VACNT foams had bulk density ~0.30 g cm^{-3} and thickness ~1.8 mm. The VACNT foams were then cut-extracted from the substrate using a custom-made core drill into 4.76 mm diameter freestanding samples for constructing the periodic array.
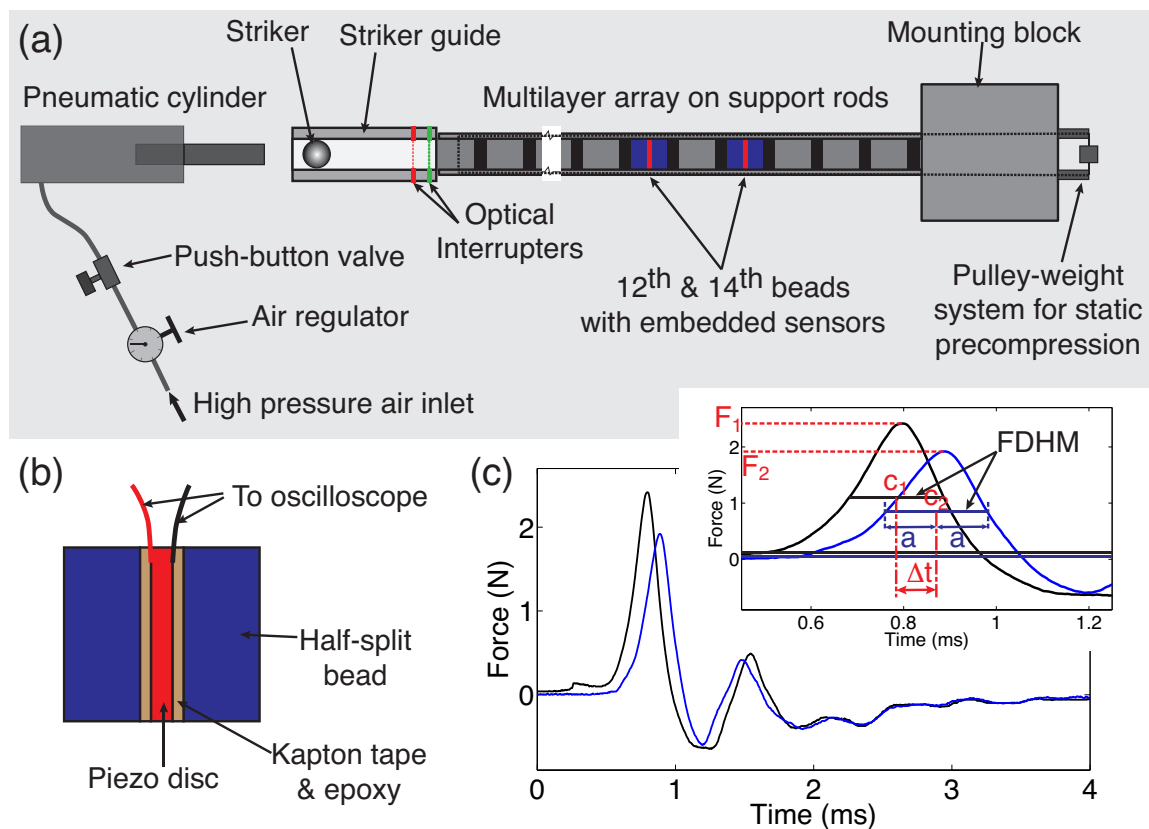
B.2.2 Wave propagation experiments

Figure B.1. Schematic of the experimental setup and data reduction method: **(a)** experimental setup showing the periodic array of VACNT foams and stainless steel cylinders, static precompression applied by the pulley-weight system, striker impact generator, optical interrupters for striker velocity measurements and the dynamic force sensors for force-time measurements, **(b)** dynamic force sensor bead with embedded piezoelectric disc **(c)** characteristic dynamic force-time profiles measured by sensors; inset shows the effective time (Δt) measurement scheme based on the full duration at half maximum method.

We assembled the one-dimensional twenty-unit cell array on four horizontal low-friction polycarbonate support rods mounted on a rigid steel block (Figure B.1(a)). Each unit cell consists of a stainless steel cylinder (*McMaster-Carr*; grade 316, length = 4.76 mm, diameter = 4.76 mm, mass = 0.677 g) and a standalone VACNT foam sample. The aligned CNT bundles in the VACNT foams were oriented along the longitudinal axis of

the one-dimensional periodic array. A precompression of 5 N was applied to the periodic array using a pulley-weight system as shown in the Figure B.1(a) to ensure that the component layers of the periodic array were fully in contact. Changing the hanging weight varied the applied precompression on the system. We excited the periodic array using striker impacts, where a spherical striker (diameter = 4.76 mm) was launched on a low friction polytetrafluoroethylene (PTFE) striker guide using a pneumatic cylinder at controlled velocities between 1 and 8 m s^{-1}. A PTFE striker (mass = 0.122 g) and a stainless steel striker (mass = 0.451 g) were used to deliver low and high amplitude force impacts, respectively. A custom-made optical interrupter built into the striker guide measured the impact velocity of the striker before the impact. When the striker interrupts the two optical paths spaced at 8.89 mm, it generates voltage signals from which the time taken for the striker to travel 8.89 mm is obtained, from which the velocity of the striker is calculated.

We embedded piezoelectric ceramic sensors into the twelfth and fourteenth beads (sensor-1 and sensor-2) to measure the dynamic force-time history of the propagating stress waves. As shown in Figure B.1 (b), the piezo discs were embedded into the half-split stainless steel cylinders using a five-minute epoxy. A thin Kapton tape layer was introduced between the piezo disc and the stainless steel cylinder to prevent any charge leakage from the piezo disc during dynamic compression. The wires from the sensors were connected to an oscilloscope using a BNC cable and the force-time history was recorded on the oscilloscope. The characteristic force-time histories recorded on the sensors 1 and 2 are shown in Figure B.1 (c).

We calculated the effective wave velocity (V_{wave}) in the one-dimensional array from the measured force-time history and the physical distance (d_{1-2}) between the two sensor beads. We used the full duration at half maximum method to calculate the effective time (Δt) taken for the wave to travel between the sensors (inset of Figure B.1 (c)). For the effective time calculations, only the first compressive segment of the recorded force pulse was considered. The centers of the half-maximum wave width were identified as the centers of the compressive pulses (c_1 and c_2). We defined the effective wave velocity as $V_{wave}=d_{1-2}/\Delta t$ and the dynamic force amplitude (F_d) as the average of the amplitudes of

the two compressive pulses ($F_d=(F_1+F_2)/2$). We plotted the effective wave velocity with the dynamic force (F_d) normalized by the static precompression (F_s) applied on the one-dimensional array.

B.3   Experimental observations and discussions

Our observations revealed an interesting trend of the effective wave velocity with the normalized dynamic force—the wave velocity reduces with the dynamic force (see the curve corresponding to F_s=5N in Figure B.2 (a)). This response suggests a softening behavior with increasing dynamic force. However, our previous studies of the constitutive responses of VACNT foams obtained in both quasistatic compression [42] and flat plunge striker impacts showed a nonlinear stiffening response [169]. It was also observed that the stress-strain responses of the VACNT foams have different loading and unloading responses with large hysteresis in both quasistatic and dynamic compressions. In addition, the loading and unloading moduli are significantly different. Such characteristics of the VACNT foams lead to softening responses when the stress-strain path transitions from the loading to unloading curve, or vice versa, with rapid convergence. This claim is supported using numerical modeling in Section B.4.

We show that the wave velocity is highly tunable over a broad range by varying the applied static precompression (Figure B.2 (a)). Varying the precompression on the periodic array compresses individual VACNT foams in the array towards the 'stiff' regions of its nonlinear stress-strain curve (Figure B.2 (b)) and as a result, increases the overall stiffness of the periodic array. As shown in the scanning electron microscope (SEM) images in Figure B.2 (c), when the VACNT foam is compressed, buckles form at the bottom 'soft' region of the sample and progresses sequentially as further compression is applied. The unbuckled region remains intact without any observable deformations as shown in the top SEM image. Due to this increasing stiffness of the periodic array, we observe that the velocity of the wave increases with increasing precompression (upward shift in curves of Figure B.2 (a), from 5N to 40N precompression).
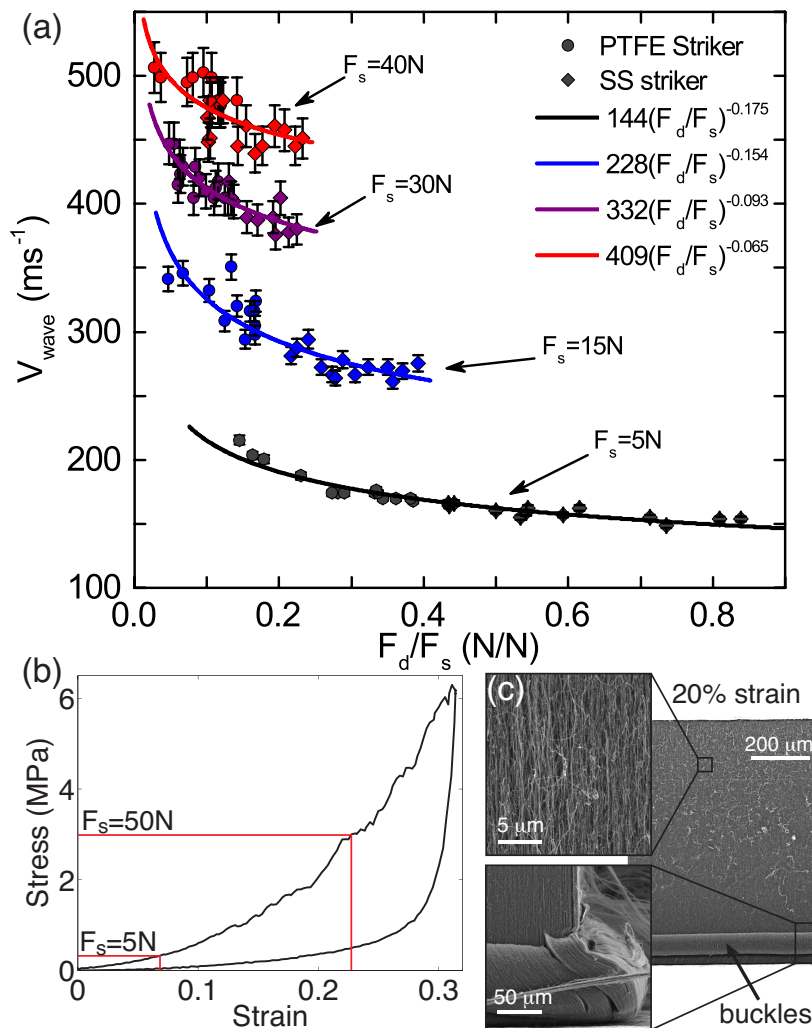
Figure B.2. (a) The variation of effective wave velocity with the dynamic force normalized by static precompression **(b)** Characteristic stress-strain response of a single layer VACNT foam in quasistatic compression cycle **(c)** Scanning electron microscope images showing the formation of buckles at the bottom 'soft' region of a VACNT foam at 0.20 strain.

B.4   Modeling and discussions

B.4.1 Proposed analytical model

We model the response of VACNT foams using a model that is similar to the Bouc-Wen model [217], which describes the hysteresis using a differential equation and results in a rate-independent force-displacement hysteresis. Our proposed model is given by

$$F(x) = \eta F_L(x) + (1 - \eta)F_U(x), \tag{B.1}$$

$$\dot{\eta} = \frac{h(\dot{x}) - \eta}{x\Lambda + x_0} |\dot{x}|. \tag{B.2}$$

Here, $F(x)$ is the force at displacement x, and F_L and F_U are the experimentally measured loading and unloading force-displacement curves. The $h(\dot{x})$ is the Heaviside step function given by,

$$h(\dot{x}) = \begin{cases} 1, & \dot{x} \geq 0 \\ 0, & \dot{x} < 0 \end{cases}. \tag{B.3}$$

The two independent parameters of the model are Λ and x_0, which control the transition speed. Equation (B.1) states that the force at any particular instance can be on the loading curve, unloading curve or somewhere in between the loading and unloading curves. Equation (B.2) states that the transition between loading and unloading is a function of the velocity ($\dot{x}$) and the transition occurs at a characteristic strain rate given by Λ. Small values of Λ result in steep spatial transitions while large values of Λ result in soft spatial transitions.

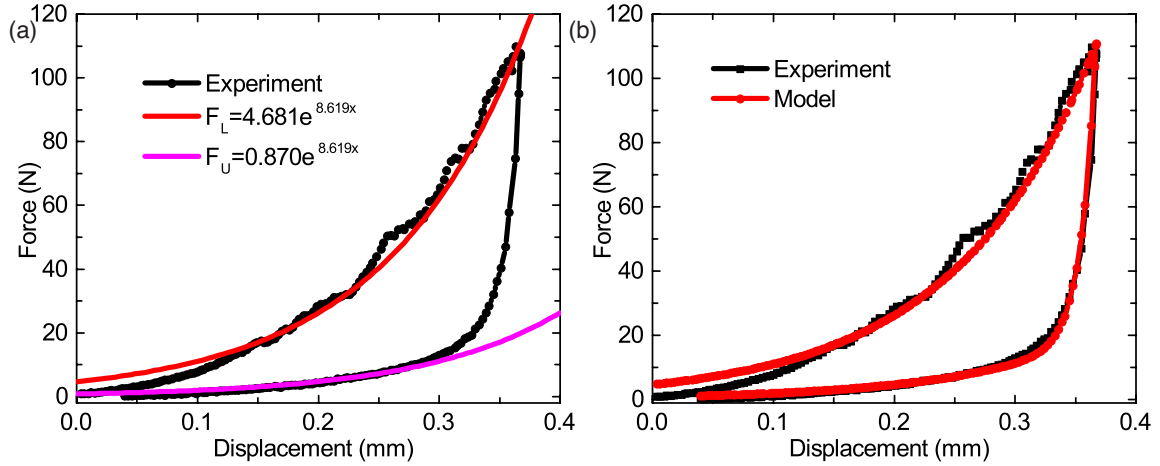## B.4.2 Numerical model and the results

Figure B.3. (a) Exponential loading and unloading curve-fits for the experimental quasistatic force-displacement curve. **(b)** The comparison of the force-displacement curves obtained from experiment and the simulated model.

We replaced the experimental quasistatic force-displacement curve with exponential fits to avoid oscillations in the response due to both the buckling events occurring in smaller length scales and the noise from the load cell. Therefore, the loading and unloading curves are given by

$$F_L(x) = Ae^{\beta x}, \tag{B.4}$$

$$F_U(x) = \alpha A e^{\beta x}. \tag{B.5}$$

The constant multiplier, A, in front of the exponential does not have any effect on the response, because it manifests as a change in the initial elongation of the nanotubes δ_0 (Equations B.6-B.8). Therefore the force depends only on the initial static force applied on the system, F_0 and the exponent, β.

$$F_L(x) = Ae^{\beta(\delta_0 + \Delta x)}, \tag{B.6}$$

$$F_0 = Ae^{\beta\delta_0}, \text{ at } \Delta x = 0. \tag{B.7}$$

Therefore,

$$F_L(x) = F_0 e^{\beta x}. \tag{B.8}$$

We used the displacements from the fitted loading and unloading curves as the input to our model. The simulated result from our model for the force-displacement curve is presented in Figure B.3(b) in comparison with the experimental force-displacement curve. It can be seen that the model is in good agreement with the experimental curve. The parameters for the fit are given in Table B.1.

Table B.1. Parameters of the model for the VACNT foams.

Λ	0.065
x_0	34.48 μm
A	4.681 N
α	0.179
β	8.619 mm^{-1}

We modeled the periodic array of stainless steel cylinders and the VACNT foams as a chain of point masses and dissipative springs such as those described by our model. The equation of motion for the ith particle is given by

$$m\ddot{x}_i = F(x_{i-1} - F_i) - F(x_i - x_{i+1}), \tag{B.9}$$

$$m\ddot{x}_0 = F_0 - k_{wire}x_0 - F(x_0 - x_1), \tag{B.10}$$

where k_{wire} is the stiffness of the wire that was used to apply the static precompression in experiments. The force F is given by the Equation B.1.

We first applied the static precompression on the sample and then simulated the transient wave propagation in the chain by specifying the initial velocities of the first particle in the chain. We obtained the force-time responses at the twelfth and fourteenth particles.

The effective wave propagation velocity was calculated from the center-to-center distance between the two particles and the time difference between the two peaks of the simulated force-time profiles. The wave velocity exhibits a slowdown effect with increasing impact force, as observed in the experiments. The qualitative comparison between the experimental and the numerical results are presented in Figure B.4. We observed from the simulations that the transition between the loading and unloading curves leads to a softening response, that results in lower wave velocities when impacted at higher striker velocities (Figure B.5). It should be noted that the prescribed initial condition η of the numerical model and the applied precompression together set the initial stress-strain state of the VACNT foams. In our simulation, we set the initial velocities of the particles to zero, and the parameter $\eta = 0.75$. Most values of η correctly reproduce the velocity slowdown. We have chosen the value of 0.75 because it results in the best qualitative agreement with the experiments. We believe that the initial value of η is a result of creep after the compression has been set.
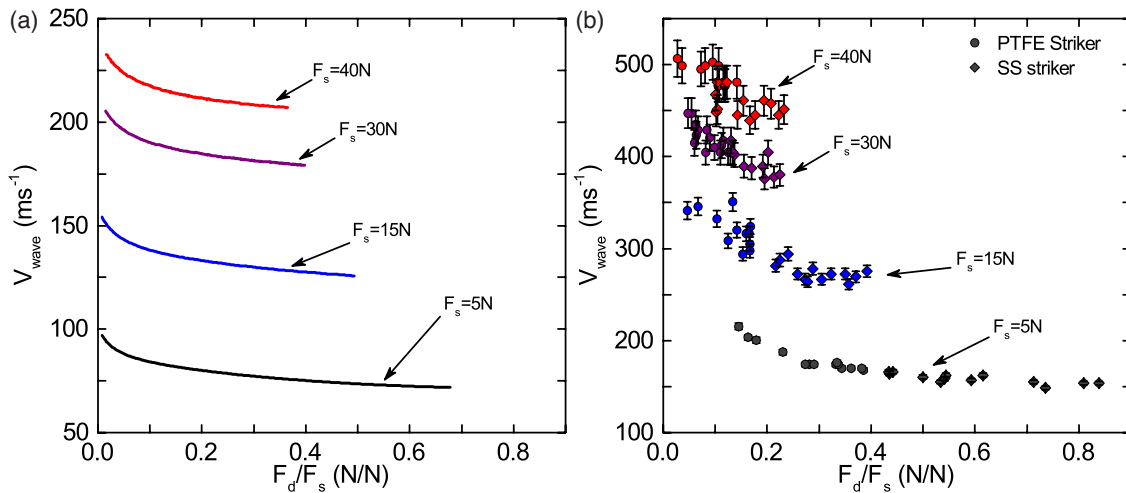

Figure B.4. A qualitative comparison between **(a)** the numerical results and **(b)** the experimental results, of the decreasing trend of the effective wave velocity at different static precompressions.
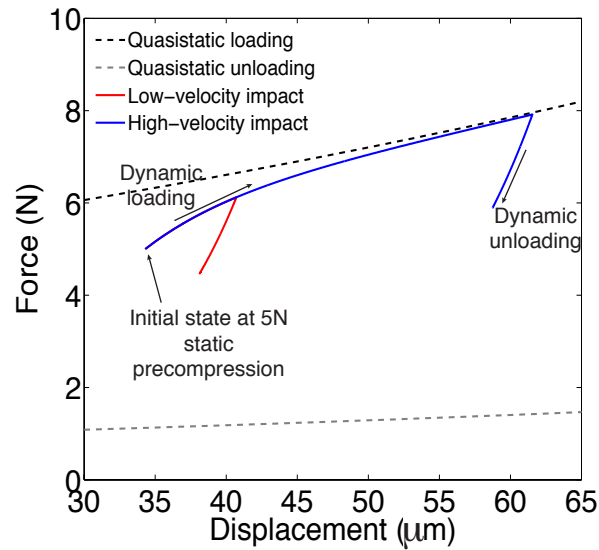
Figure B.5. The dynamic loading-unloading response of a VACNT foam during the transient excitation of the periodic array, showing the softening response.

In addition, the wave velocity increases when the precompression is increased, reproducing the experimental observations. However, the model does not show quantitative agreement with the experiments for the velocities predicted. When the exponent β of the model is increased to 34.48 mm^{-1} and the x_0 is reduced to 4.31 μm, keeping all the other parameters constant, the model predicted results that are in good quantitative agreement with the experiments. The reasons for this quantitative discrepancy between the model and the experiments are unclear. However, the model is extremely simple and correctly explains the velocity slowdown effect, which is the novelty of the experiments. We have neglected many other experimental issues such as friction between the support rods and the periodic array, strain rate effects and preconditioning of the nanotubes.
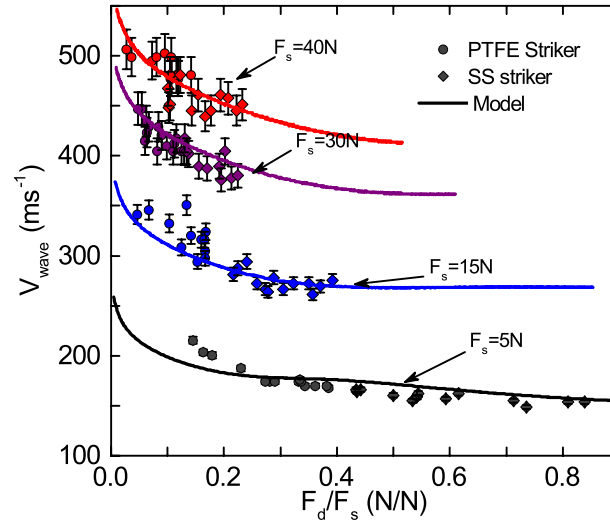
Figure B.6. Comparison of the numerical results with experimental results, of the decreasing trend of the effective wave velocity at different static precompressions, calculated for $\beta=34.48$ mm^{-1} and $x_0=4.31$ μm.

B.5   Conclusions

We have experimentally studied the wave propagation in a periodic array of VACNT foams alternated with stainless steel interlayers, subjected to transient excitations. We show a unique response, where the effective velocity of the propagating wave decreases with the increasing impact force. The wave velocity is also highly tunable over a broad range using a static precompression applied to the array. We developed an analytical model with rate-independent hysteresis for the VACNT foams. We modeled the periodic array using a chain of masses connected by the developed VACNT foam model and qualitatively show the wave slowdown effect. We showed that the wave slowdown effect arises from the softening response of VACNT foams that occurs when transitioning between loading and unloading curves with large hysteresis.